

DAVID W. 11-4171

UNITED STATES DEPARTMENT OF COMMERCE

1971

WHEEL ASSEMBLY
MOTOR VEHICLE
DIVISION

14000 Townsley State Street
San Francisco, California 94124

UNIT STATES DEPT.

OF COMMERCE

WASHINGTON, D.C. 20540

SEMI-ANNUAL REPORT - CONTACT DIVISION 72-5-0103

Approved for public release; distribution unlimited.

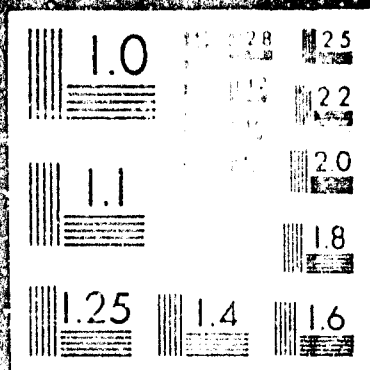
Prepared for:

ARMY MATERIALS AND MECHANICS RESEARCH CENTER
WATERLOO, MASSACHUSETTS 02127

NATIONAL DEFENSE
INFORMATION SERVICE

SEE PD 308 434

AD
738564



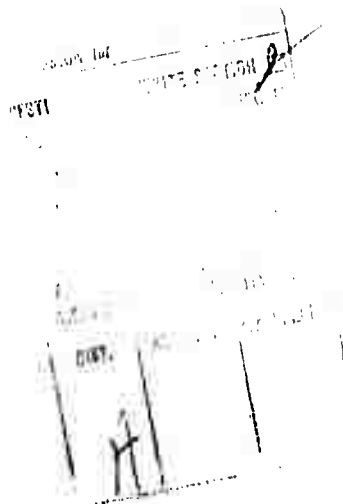
**BEST
AVAILABLE COPY**

The findings in this report are not to be construed as an official Department of the Army position, unless so designated by other authorized documents.

Mention of any trade names or manufacturers in this report shall not be construed as advertising nor as an official indorsement or approval of such products or companies by the United States Government.

DISPOSITION INSTRUCTIONS

Destroy this report when it is no longer needed.
Do not return it to the originator.



Unclassified

Security Classification

DOCUMENT CONTROL DATA - R & D

(Security classification of title, body of abstract and indexing annotation must be entered when the overall report is classified)

1. ORIGINATING ACTIVITY (Corporate author) TRW INC. TRW Systems Group One Space Park Redondo Beach, California		2a. REPORT SECURITY CLASSIFICATION Unclassified	
3. REPORT TITLE NONDESTRUCTIVE TESTING USING TRW ACOUSTO-OPTICAL IMAGING SYSTEM		2b. GROUP	
4. DESCRIPTIVE NOTES (Type of report and inclusive dates) Semi-Annual Report 30 June 1970 to 1 July 1971			
5. AUTHOR(S) (First name, middle initial, last name) Robert Aprahamian Jerold L. Jacoby Pravin G. Bhuta			
6. REPORT DATE August 1971		7a. TOTAL NO. OF PAGES 49	7b. NO. OF REFS 8
8a. CONTRACT OR GRANT NO. DAAG46-70-C-0103		9a. ORIGINATOR'S REPORT NUMBER(S) AMMRC CR 71-4/2	
b. PROJECT NO. ARPA 1245		9b. OTHER REPORT NO(S) (Any other numbers that may be assigned this report)	
10. DISTRIBUTION STATEMENT Approved for public release; distribution unlimited.			
11. SUPPLEMENTARY NOTES		12. SPONSORING MILITARY ACTIVITY Army Materials and Mechanics Research Center, Watertown, Massachusetts 92172	
13. ABSTRACT The technique of Acousto-Optical Imaging (AOI) enables one to "see", on a real-time basis, within optically opaque materials and to detect internal or surface flaws and/or other irregularities which might be present. The process uses an ultrasonic beam to probe the object under study. As it interacts with the object, the ultrasonic beam acquires an acoustical "picture" of the object. The acoustic waves then interact with a monochromatic light beam (as from a laser). Optical sidebands are produced by the Bragg diffraction of light. The cumulative result of this process is that these sidebands produce a visual image of the interior of the object. This report discusses the results of an analytical and experimental study to evaluate the applicability of acousto-optical imaging to nondestructive testing. In addition to the determination of the system resolution, the effects of specimen thickness, geometry, composition and surface roughness were investigated. A new technique which utilizes the sound reflected from the specimen to obtain an acousto-optical image was also developed. Results using this technique to detect known surface flaws on a specimen are in good agreement with the actual flaws.			

~~Unclassified~~
~~Security Classification~~

KEY POINTS

Ultrasonic Frequencies
Acoustics
Nondestructive Tests
Images

[illegible]

1

AMMRC CR 7104/2

NONDESTRUCTIVE TESTING USING TRW ACOUSTO-OPTICAL IMAGING SYSTEM

Robert Aprahamian
Jerold L. Jacoby
Pravin G. Bhuta

Advanced Technology Staff Group
Space Vehicles Division
TRW SYSTEMS GROUP
One Space Park
Redondo Beach, California

August 1971

Details of illustrations in
this document may be better
studied on microfiche

Semi-Annual Report - Contract DAAG46-70-C-0103

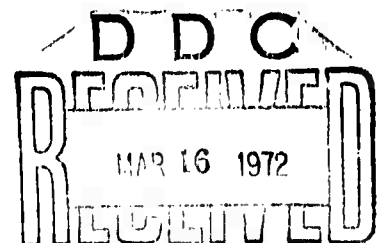
ARPA 1245

ARPA - NDT Research

Approved for public release; distribution unlimited.

Prepared for

ARMY MATERIALS AND MECHANICS RESEARCH CENTER
Watertown, Massachusetts 02172



A

ARMY MATERIALS AND MECHANICS RESEARCH CENTER

NONDESTRUCTIVE TESTING USING
TRW ACOUSTO-OPTICAL IMAGING SYSTEM

ABSTRACT

The technique of Acousto-Optical Imaging (AOI) enables one to "see", on a real-time basis, within optically opaque materials and to detect internal or surface flaws and/or other irregularities which might be present. The process uses an ultrasonic beam to probe the object under study. As it interacts with the object, the ultrasonic beam acquires an acoustical "picture" of the object. The acoustic waves then interact with a monochromatic light beam (as from a laser). Optical sidebands are produced by the Bragg diffraction of light. The cumulative result of this process is that these sidebands produce a visual image of the interior of the object. This report discusses the results of an analytical and experimental study to evaluate the applicability of acousto-optical imaging to nondestructive testing. In addition to the determination of the system resolution, the effects of specimen thickness, geometry, composition and surface roughness were investigated. A new technique which utilizes the sound reflected from the specimen to obtain an acousto-optical image was also developed. Results using this technique to detect known surface flaws on a specimen are in good agreement with the actual flaws.

FOREWORD

The work reported was performed by the Advanced Technology Staff Group of Space Vehicles Division, TRW Systems, Redondo Beach, California. It was sponsored by the Advanced Research Projects Agency (ARPA Order No. 1245). It was performed under Army Materials and Mechanics Research Center Contract No. DAAG46-70-C-0103 with Mr. O. R. Gericke, Chief, Nondestructive Testing Branch, AMMRC, as technical monitor. Project Manager at TRW Systems was Mr. R. Aprahamian with technical support provided by Mr. J. L. Jacoby, Dr. P. G. Bhuta and Mr. C. V. Murrow. The authors wish to thank Mr. O. R. Gericke for his very valuable help and suggestions throughout the course of this investigation.

TABLE OF CONTENTS

	Page
ABSTRACT	11
FOREWORD	111
INTRODUCTION.	1
ACOUSTO-OPTICAL IMAGING	1
RESOLUTION MEASUREMENTS	7
DETECTABLE FLAW SIZE.	18
THREE-DIMENSIONAL CHARACTER OF A FLAW	20
SURFACE ROUGHNESS	25
SPECIMEN GEOMETRY	28
COMPOSITE SPECIMEN.	33
ACOUSTIC MICROSCOPE	34
REFLECTED SOUND IMAGING	37
CONCLUSIONS	41
REFERENCES.	42

INTRODUCTION

Acousto-optical Imaging (AOI) is a technique enabling one to "see", on a real-time basis, within optically opaque materials and to detect internal or surface flaws and/or other irregularities which might be present. The process uses an ultrasonic beam to probe the object under study. The ultrasonic beam, as it interacts with the object, acquires an acoustical "picture" of the object. After passing through the object, the acoustic waves interact with a beam of monochromatic light. Due to Bragg diffraction optical sidebands are produced. If one of the sidebands is projected onto a screen or TV camera, an optical image of the interior of the object is seen.

The objective of this investigation was to further examine the general applicability of the TRW acousto-optical imaging system to non-destructive testing. The acousto-optical imaging apparatus was obtained and preliminary tests, to establish the validity of the technique, were performed under TRW company-sponsored programs prior to initiation of this ARPA sponsored work. The current investigation included an experimental study to determine the capabilities and limitations of the underlying Bragg diffraction principle upon which the imaging system is based. Factors which influenced the performance of the system were identified to optimize the system. Using carefully prepared control test specimens containing flaws, whose locations and dimensions were known, the performance of the system was measured. A series of tests were performed to measure the resolution at acoustic frequencies ranging from 4 to 40 MHz. The experimental results from the resolution tests were compared with theoretical predictions and were found to be in good agreement.

Further experimental tests investigated the effects of varying degrees of surface roughness and specimen geometry on the ability of the system to produce usable images. The ability to determine the three-dimensional character of a flaw and to detect an unbonded area in a composite specimen were demonstrated. An analysis was performed which considered the design of an acoustic microscope based upon the acousto-optical imaging technique. Finally, preliminary tests were performed to obtain an acousto-optical image using the sound reflected from the object. Pulsed light and sound sources were synchronized to "range-gate" the object. Images were obtained of a surface flaw on the front side of a sample of borsic aluminum.

ACOUSTO-OPTICAL IMAGING

TRW's acousto-optical imaging system employs ultrasound to acquire an acoustical "picture" of an object. A visual image is extracted from the ultrasound using the principle of Bragg diffraction of light.¹ Figure 1 shows schematically a typical laboratory setup used for this system.

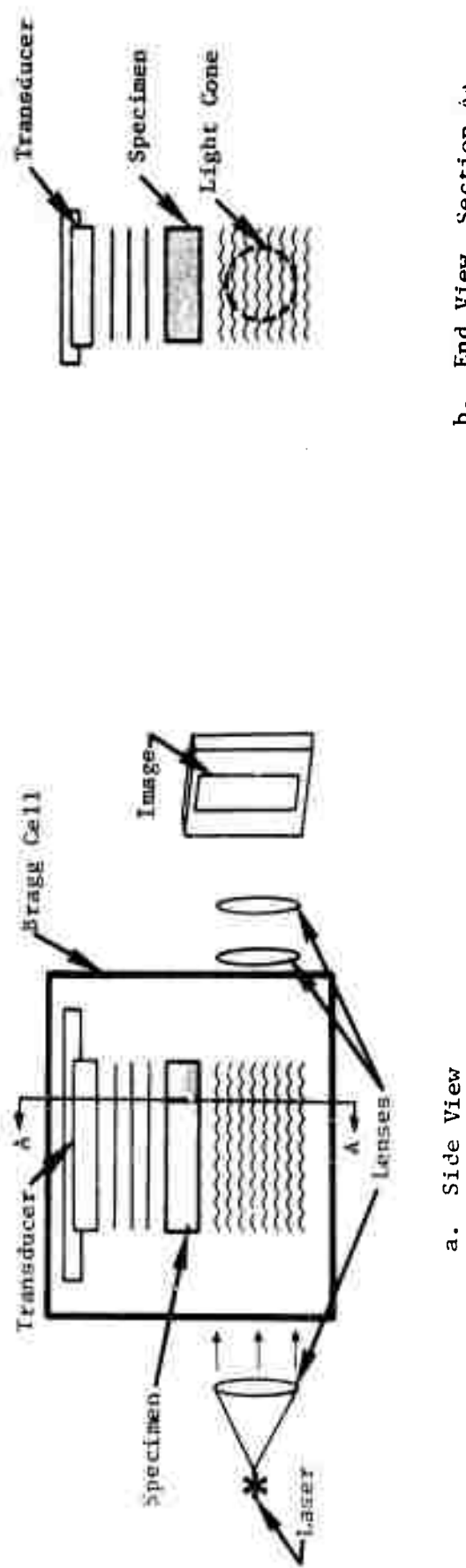


Figure 1: Experimental configuration for acousto-optical imaging

Referring to Figure 1, an object is placed in a tank containing a good acoustic wave transmitter such as water. The tank is referred to as a wave coupler or Bragg cell. An ultrasonic transducer is placed on one side of the Bragg cell. This transducer emits a plane acoustic wave which interacts with the object. X-cut quartz transducers were used as the acoustic sources in this investigation. The transducers measure about 1" x 1-1/4" and are air-backed. Figure 2 shows a photograph of one of these transducers and also a diagram depicting its construction. Two transducers, having fundamental frequencies of 4 MHz and 8 MHz were used. They were used in their fundamental and also at their odd harmonics. That is, the 4 MHz transducer was used at 4, 12, 20 and 28 MHz and the 8 MHz transducer was used at 8, 24 and 40 MHz.

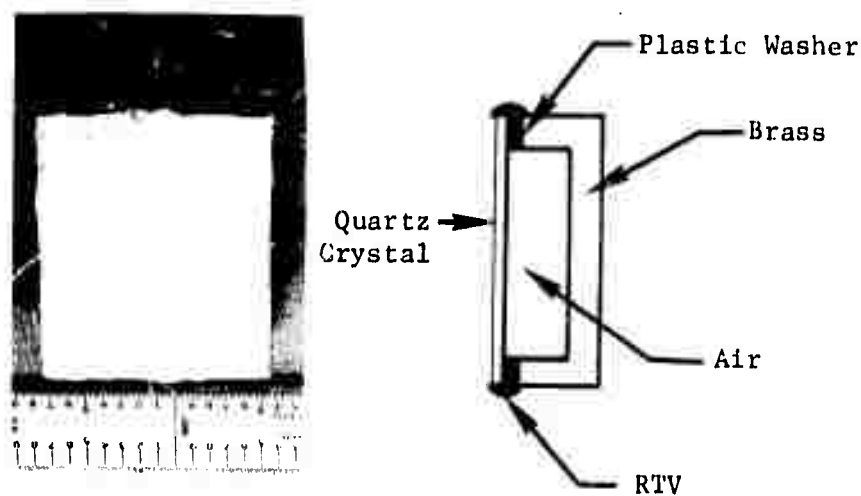


Figure 2: X-cut quartz transducer used for these experiments

That part of the acoustic wave which is transmitted through the object is distorted so that it carries with it an acoustic image of the interior of the specimen. The acoustic waves, having passed the object, propagate through the path of the light. Except as noted, the light source used in this investigation was a 50 mw HeNe laser ($\lambda = 6328\text{\AA}$). The light is passed through the Bragg cell in the shape of a cone whose axis is approximately orthogonal to the direction of propagation of the acoustic waves. Since the acoustic waves are composed of regions of compression and relief or, equivalently, regions of varying indices of refraction,

they act as an ordinary moving diffraction grating to the light causing optical sidebands to be produced. The sidebands created by this process diverge angularly from the undisturbed light cone. After exiting the Bragg cell, one sideband (usually the one closest to the carrier) interacts with a set of optics arranged in a telescope configuration causing a magnification of the beam. This sideband is then projected onto a viewing screen (or TV vidicon) allowing an image of the interior of the object to be seen. Ideally, as much optical energy as possible should be channeled into the sideband used for imaging. However, in practice not all the available optical energy can be channeled into one sideband, but it is possible to favor one sideband over others.

Bragg's law expresses the condition for which one sideband will be favored for constructive interference. Mathematically, this condition is expressed as¹

$$\sin \theta_B = \frac{N\lambda}{2\Lambda} \quad (1)$$

where

θ_B = Bragg angle (the angle between the light and sound propagation vectors is $90^\circ - \theta_B$)

N = integer

λ = wavelength of light

Λ = wavelength of sound

In this investigation, the geometry was arranged so that the Bragg condition would favor the sideband closest to the carrier ($N = 1$).

The sensitivity and resolution of the system are two parameters of particular interest in nondestructive testing applications. For this study, sensitivity is defined to be the minimum sound intensity present in the Bragg cell to produce a usable image. The resolution is defined to be the ability to distinguish closely spaced objects. These parameters measure the ability of the system to detect flaws in a specimen.

Four factors influence the sensitivity of the system. They are: (1) the intensity of the light source (laser), I_0 , (2) the interaction distance between the light and sound, l , (3) the efficiency of the coupling medium with respect to water², M_w^* ; and, (4) the intensity of the sound in the volume of the light-sound interaction, P . These factors

are related by Equation 2:²

$$I = I_0 \sin^2 (1.4d \sqrt{M_w P}) \quad (2)$$

where I is the image intensity.

The quartz crystals used with this system produce a collimated acoustic wave. The maximum interaction distance, l , is the width of the acoustic column. The efficiency of the coupling medium is given by the figure of merit, M_w . As is seen in Table I, the figure of merit may vary over a large range of values, however, it happens that water is a very good coupling medium. The sound intensity is determined by the output of the sound source (transducer) and the energy loss before the sound reaches the interaction area. The minimum intensity, I , which can be observed visually as a real-time image is³

$$I_{\min} = 2.2 \times 10^{-6} \text{ watts/cm}^2$$

For this study, values of the factors in Equation 2 were: $I_0 = 4.4 \times 10^{-3}$ watts/cm; $l = 2.54$ cm; and $M_w = 1.0$. Thus, a minimum acoustic intensity in the light-sound interaction zone of 4×10^{-5} watts/cm² were necessary to yield a visual image.

The resolution of the Acousto-Optical Imaging system is ultimately limited by diffraction effects in both the acoustic and optical waves. Factors influencing the resolution include the arrangement and resolution of the optical system, the arrangement of the object in the acoustic medium relative to the interaction volume, the size and shape of the interaction volume, and the acoustic wavelength.

The factors cited above for determining the sensitivity and resolution of the system can be divided into two main groups. The first

$$*M_w = \frac{M}{M_{H_2O}} \quad \text{where } M = n^2 p^2 / v^2 \rho,$$

n = refractive index of the coupling medium
 p = elastooptic coefficient
 v = sound velocity
 ρ = density

and M_w is defined as being equal to 1.0 for water.

TABLE I²

Comparison of the Efficiency of the
Coupling Medium for Various Materials

<u>Material</u>	<u>M_w</u>
Water	1.0
Dense Flint Glass	0.06
Extra-Dense Flint Glass	0.12
Fused Quartz (SiO ₂)	0.006
Polystyrene	0.8
KRS-5	1.6
Lithium Niobate (LiNbO ₃)	0.012
Lithium Fluoride (LiF)	0.001
Rutile (TiO ₂)	0.001
Sapphire (Al ₂ O ₃)	0.001

group influences the hardware design of the AOI system. When these factors are optimized and built into the system, it can be expected that they will remain fixed. These factors include the intensity of the light source, the maximum power available to drive the transducer, the coupling medium, and the size and shape of the light-sound interaction volume. The size and shape of the light-sound interaction volume can be altered by providing the ability to change optical components. However, by proper design this need could be minimized.

The second group of system variables relate not to the construction of the system, but how it is to be used to perform a particular function. For example, the sensitivity is, in part, determined by the sound intensity at the interaction volume. The attenuation of the sound in the water medium is therefore a major factor in determining the sensitivity. (The characteristic attenuation distance of an 11 Megahertz acoustic wave in water at 20°C is 6 in., Ref. 4.) The attenuation is exponential with

the distance and the square of the frequency ($P = P_o e^{-\alpha(v^2)x}$). Thus, it would appear that greater sensitivity can be obtained by placing the transducer close to the light-sound interaction volume (if object geometry permits) thereby reducing the acoustic path, x , and also by using lower frequency sound, v .

The resolution of an acoustic system is dependent on the acoustic wavelength. The resolution can be increased by using sound having a shorter wavelength, i.e., higher frequency. But this violates the sensitivity condition. Clearly, to optimize the system performance, a tradeoff between these two requirements must occur. This can be accomplished by taking into account the attenuation for a particular situation and the resolution required.

In order to properly evaluate the capabilities and limitations of an imaging system, it is necessary to have a set of standards such that the data can be expressed in quantitative form. Tests using naturally occurring flaws in materials are valid only to the extent that the character of the flaw can be verified by alternate methods. In some cases, it may be difficult to find flawed specimens exhibiting the desired characteristics. The approach to this problem which was followed for this study, was to fabricate all of the control specimens to the desired specifications. In this manner, the extent and character of the flaw was known to a considerable precision.

While the outstanding feature of the AOI system is that it produces real-time images, it is also necessary that a good photographic record be obtained. In this way, test results can be reported, compared and saved for future reference. Difficulties in photographing images are often encountered when laser light is used (as in holography). This is a consequence of the granular nature of laser light. It is often found that a good, real-time image will not produce a good photograph; in other cases, the photograph is better. A variety of different photographic techniques have been applied to the recording of AOI images. These have included a number of different optical arrangements, cameras, films and development processes. One of the more successful techniques, and by far the easiest and fastest, involves the use of Polaroid film. The screen which is normally used to display the real image is replaced by the film packet. The packet is opened in the darkened room and the laser shuttered to provide the proper exposure. The film is exposed directly by the AOI image. No "camera" or other focusing optics are needed. The images presented in this report, with the exception of those in the Reflected Sound Imaging section, were recorded by this method on Polaroid Type 52 and Type 55 P/N films (Type 55 P/N provides both a positive print and a negative).

RESOLUTION MEASUREMENTS

In this section, the results of a combined analytical and experimental study of the system resolution are reported and evaluated. For this study, the resolution was arbitrarily defined as being the dimensions of the smallest set of holes drilled into a specially prepared specimen which can be imaged in a way that each individual hole is discernable from the image. This specimen, shown in Figure 3, consists of a flat



Reproduced from
best available copy.

Figure 3: Resolution test specimen. Hole diameters (in inches) are indicated below each set of holes.

aluminum plate (0.125" thick) with a series of holes drilled into it from one side. The hole diameters are 0.110", 0.055", 0.028" and 0.0135". There are four holes of each size and the separation between these holes is equal to the hole diameter. Machining tolerances on this specimen were held to ± 0.001 ". Images of these holes were obtained at 4, 8, 12, 20, 24, 28 and 40 MHz. The resulting images are shown in Figures 4 through 7. Each figure depicts a different set of holes imaged at the frequencies delineated above. (Note: The .0135" holes (Figure 7) could not be resolved at the lower frequencies and hence are not included.)

The ability to resolve the individual holes from their image is limited by at least two effects, (i) the resolution of the light-sound interaction and (ii), the diffraction of the sound by the small drilled holes in the specimen. The theoretical and resolution limit for the light-sound interaction is given by (Ref. 5)

$$d = (2m/\pi\phi)\Lambda \quad (3)$$

where

n = index of refraction of water

λ = light cone convergence angle (.093 radians for our tests)

Λ = acoustic wavelength in water

4 MHz crystal transducer

a. 4 MHz



c. 12 MHz



d. 20 MHz



f. 28 MHz



8 MHz crystal transducer

b. 8 MHz



Reproduced from
best available copy.

e. 24 MHz



g. 40 MHz



Figure 4: Acousto-optical images at various frequencies of four 0.110" diameter holes

4 MHz crystal transducer

a. 4 MHz



c. 12 MHz



d. 20 MHz



f. 28 MHz



Reproduced from
best available copy.

8 MHz crystal transducer

b. 8 MHz



e. 24 MHz



g. 40 MHz



Figure 5: Acousto-optical images at various frequencies of four 0.055" diameter holes

4 MHz crystal transducer

a. 4 MHz



c. 12 MHz



d. 20 MHz



f. 28 MHz



8 MHz crystal transducer

b. 8 MHz



Reproduced from
best available copy.

e. 24 MHz



g. 40 MHz



Figure 6: Acousto-optical images at various frequencies of four 0.028" diameter holes

4 MHz crystal transducer

8 MHz crystal transducer

a. 12 MHz



b. 20 MHz



d. 28 MHz



Reproduced from
best available copy.

c. 24 MHz



e. 40 MHz



Figure 7: Acousto-optical images at various frequencies of four 0.0135" diameter holes

In this equation, d is defined as the minimum resolvable linear dimension in the plane orthogonal to the line axis of the light beam, (i.e., d is the theoretical resolution along the vertical axis of the images in Figures 4-7). The validity of Equation 3 can be determined with the aid of Figures 4-7. For example, for a frequency of 4 MHz, the theoretical resolution limit, d , is 0.131". The largest hole diameter is 0.110". As this is smaller than d , one would not expect to be able to resolve a clear image of any of the holes at this frequency. This lack of resolution is evident in the figures. At 12 MHz, the theoretical resolution is 0.0437". As expected, the 0.110" diameter holes are clearly resolved. The images of the 0.055" and the 0.028" diameter holes show diffraction effects. It is difficult to distinguish the hole boundaries and it appears that five or more holes are present. (This is discussed in greater detail below.) The 0.0135" diameter holes are not resolved at this frequency.

The resolution limit, d , (from Equation 3) is plotted vs. acoustic frequency in Figure 8. The resolution of the images in Figures 4 through 7 were rated by several individuals within the laboratory. The position where each image falls on the graph in Figure 8 has been noted by its rating: G = Good; F = Fair, P = Poor. Equation 3 predicts that we will be able to resolve the drill holes in those images which fall above the line in Figure 8. For the images below the line, it is expected that the drill holes would be indistinguishable. It can be seen from Figures 4-7 that our results are in general agreement with these predictions.

In several of the images, particularly those which fall near the line in Figure 8, it is difficult to determine the boundaries of the holes. In some of the pictures, it appears that more than four holes are present. These effects are due to the diffraction of the sound by the holes in the specimen. Diffraction effects are not important if $\lambda_s/a \ll 1$ (where λ_s is the acoustic wavelength in the specimen and a is the hole diameter). For these experiments, λ_s is on the same order as a and thus the diffraction of sound by the drilled holes is a significant factor in the resolution of the system.

To determine the effects of acoustic scattering, a comparison was made between the apparent size of one set of holes as determined from the acousto-optical image and the actual specimen dimensions. For this purpose, the .055" diameter holes shown in Figure 5 were used. To arrive at the size of the holes from the acousto-optical image, one must consider the magnification inherent in the acousto-optical imaging process. The magnification factor was obtained by measuring the distance between the center lines of the two outer holes in the acousto-optical image and comparing it with the actual distance between the holes measured from the specimen, see Figure 9. The magnification factor, given

G = Good
F = Fair
P = Poor

$$d = \frac{2n}{\pi \phi} \lambda = \frac{2nv}{\pi \phi \nu}$$

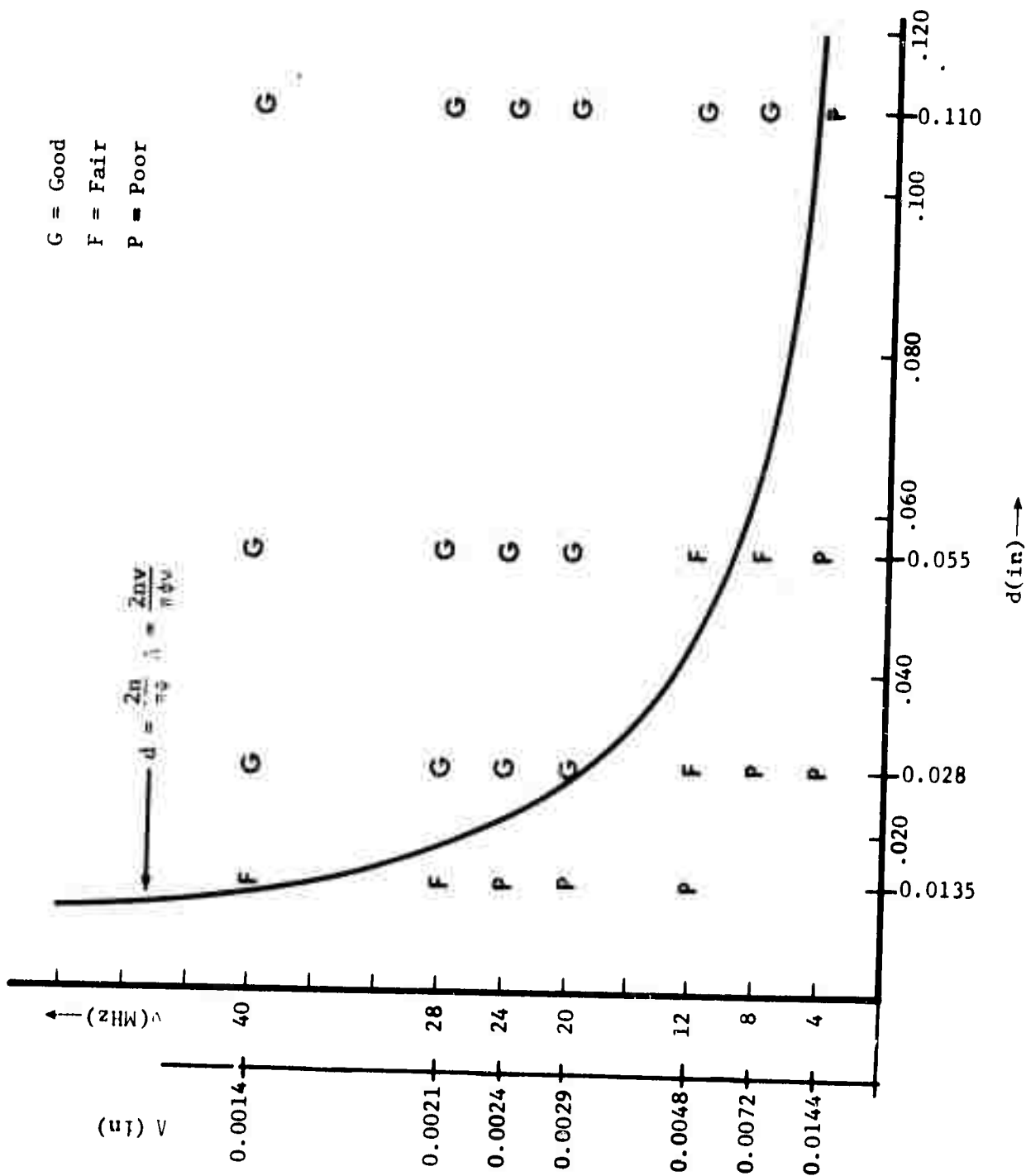


Figure 8: Resolution limit, d , vs. acoustic frequency, ν . The letters indicate the appropriate positions of the images in Figures 4-7 and signify the quality of each image

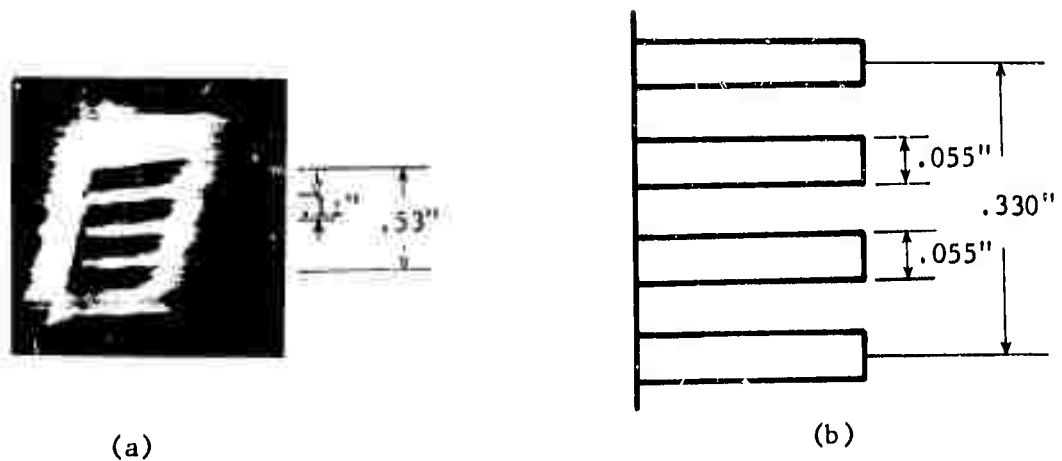


Figure 9: Comparison of AOI image with actual specimen dimension for .055" diameter holes imaged at 24 MHz
 (a) Acousto-optical image
 (b) Schematic of actual specimen

by the ratio of the image size to the actual specimen size is $\frac{0.53" \pm 0.02"}{0.330" \pm .0001"} =$

1.6 ± 0.1 . The error band, $\pm 0.02"$, assigned to the acousto-optical image measurement is obtained from the optical resolution limit, d , discussed previously (Equation 3). The tolerance, $\pm 0.001"$, is the tolerance held by the machinist in fabricating the specimen. Having this magnification factor, the "apparent" hole diameter as indicated by Figure 9 is $\frac{0.11" \pm 0.02"}{1.6 \pm 0.1} = .069" \pm 0.17"$. The actual hole size,

.055", is within the error band of the measured value. This comparison however, assumes the information contained in the acoustic wavefronts accurately defines the holes. This, however, is not the case as can be shown using diffraction theory (Ref. 6). It can be shown that the amplitude of acoustic pattern for a plane wave interacting with four opaque strips of infinite extent is given by

$$\begin{aligned}
u(x_o, y_o, z_o) = & \frac{e^{ikz_o}}{i\Lambda z_o} \int_{-\infty}^{\infty} e^{\frac{ik}{2z_o}(y_1 - y_o)^2} dy_1 \cdot \\
& \left[\int_{-\infty}^{-\frac{7a}{2}} e^{\frac{ik}{2z_o}(x_1 - x_o)^2} dx_1 + \int_{-\frac{5a}{2}}^{-\frac{3a}{2}} e^{\frac{ik}{2z_o}(x_1 - x_o)^2} dx_1 \right. \\
& + \int_{-\frac{a}{2}}^{\frac{a}{2}} e^{\frac{ik}{2z_o}(x_1 - x_o)^2} dx_1 + \int_{\frac{3a}{2}}^{\frac{5a}{2}} e^{\frac{ik}{2z_o}(x_1 - x_o)^2} dx_1 \\
& \left. + \int_{\frac{7a}{2}}^{\infty} e^{\frac{ik}{2z_o}(x_1 - x_o)^2} dx_1 \right] \quad (4)
\end{aligned}$$

where

$u(x_o, y_o, z_o)$ = amplitude of acoustic field at x_o, y_o, z_o

k = acoustic wave number = $\frac{2\pi}{\Lambda}$

a = width of acoustically opaque strip

The limits of integration are depicted in Figure 10. The acoustic intensity pattern, $I(x_o, y_o, z_o)$, is given by

$$I(x_o, y_o, z_o) = |u(x_o, y_o, z_o)|^2 \quad (5)$$

The integrals given in Equation (4) were solved numerically. The intensity distribution, $I(x_o)$, as plotted by a computer for the conditions under which the experiments were performed i.e.,

$$\Lambda_s = 0.007''$$

$$a = 0.055''$$

$$z_o = 1.0''$$

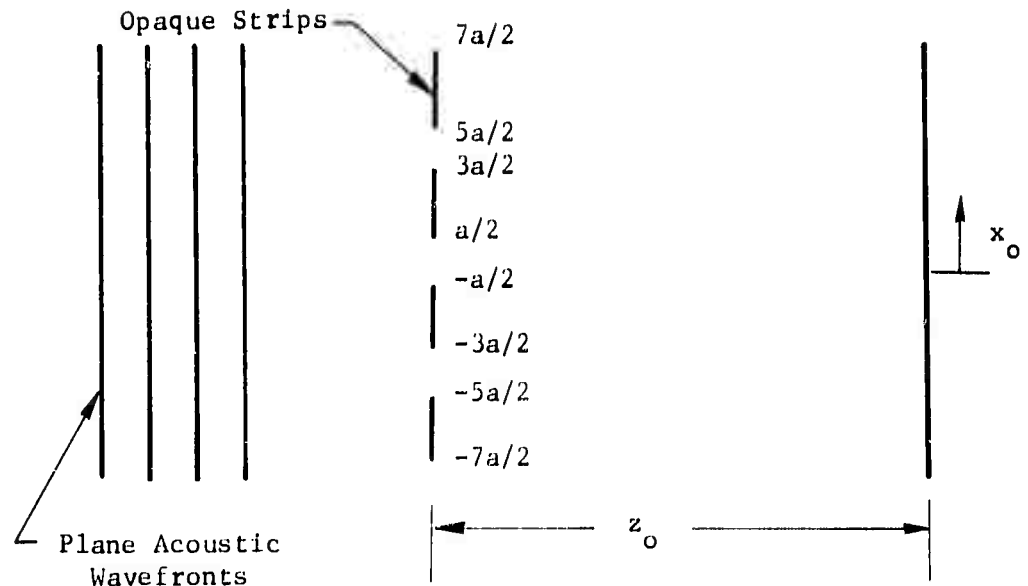


Figure 10: Diffraction of acoustic waves by four acoustically opaque strips

is shown in Figure 11. The range of x_0 on this plot is $x_0 = \pm 0.50''$. The four deep dips in the curve represent shadows in the intensity field

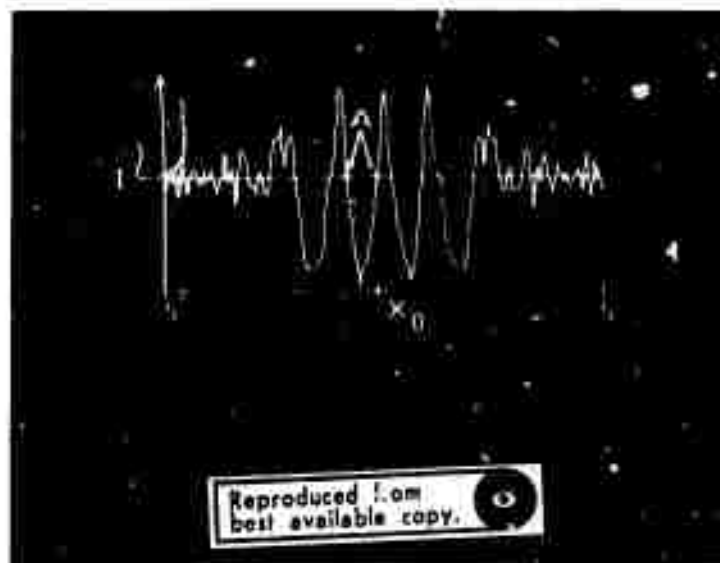


Figure 11: Acoustic intensity pattern (plotted by computer) of a plane wave diffracted by four acoustically opaque strips

behind the opaque strips. In the acousto-optical images they appear black and represent the four drilled holes. The width of these shadowed regions (measured between points A on Figure 11) measures $0.074'' \pm .004''$ indicating an "apparent" hole diameter of $0.074''$. This value is very close to the hole sizes indicated by the acousto-optical images (i.e., $0.074''$ vs $0.069''$). This indicates that the Bragg diffraction process accurately reconstructs the acoustical picture, however, the acoustical picture may not accurately describe the flaw because of acoustic diffraction effects.

In summary, the following measurements were made of the four $0.055''$ diameter holes imaged at 24 MHz.

<u>Method of Measurement</u>	<u>Measured Hole Diameter</u>
Actual Specimen Size	$0.055'' \pm 0.001''$
Calculation of Four Opaque Strip Diffraction Pattern	$0.074'' \pm 0.004''$
Measurement from AOI	$0.069'' \pm 0.017''$

DETECTABLE FLAW SIZE

In the preceding section, the ability of the acousto-optical system to resolve a flaw was discussed. It was shown that the resolution of the system was more strongly limited by acoustic diffraction effects than by the Bragg diffraction process. However, each case considered in which the flaws were judged to be unresolved, the existence of the flaws was clearly evident. The ability to detect, rather than resolve a flaw is a less stringent requirement, but nevertheless, is still often useful in nondestructive testing.

From the resolution analysis (preceding section), it was concluded that the four $0.0135''$ diameter holes could not be resolved below 28 MHz. However, it will be shown that a single $0.0135''$ hole can be clearly resolved, or detected, at 12 and 20 MHz. A calibration specimen similar to the one described in Section 3.0 was fabricated; the change being that single holes rather than groups of four holes were drilled. The dimensions of the single holes are the same as in the previously described specimen. Figure 12 shows acousto-optical images of the $.0135''$ hole at 12 and 20 MHz. Diffraction effects are evident in the figure by the appearance of more than one line. These effects, however, do not hinder, but often aid, the detection of a flaw. Figures 7a and 7b of the four $0.0135''$ holes are duplicated in Figure 12 for purposes of comparison.

As it is not practical to machine smaller flaws, further tests were conducted using lengths of stainless steel wire stretched between



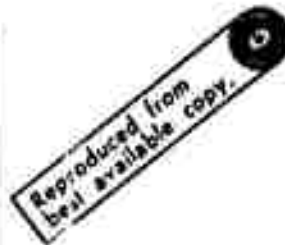
a) Four holes, 12 MHz



c) Single hole, 12 MHz



b) Four holes, 20 MHz



d) Single hole, 20 MHz

Figure 12: Acousto-optical images of 0.0135" diameter holes drilled into an aluminum specimen. The images in a) and b) (duplicates of Figures 7a and 7b) are of four holes. The images in c) and d) are of a single hole.

two supports (Figure 13). Images were obtained of wires having diameters of 0.008", 0.006" and 0.003" using 12 MHz and 20 MHz ultrasound. The acousto-optical images of these wires are shown in Figure 14. At 20 MHz, the 0.008" and 0.006" wires are easily detected, however, the 0.003" wire was not. At 12 MHz, the 0.006" wire is difficult to image and the 0.003" wire is almost undetectable from the photograph. Hence, the detection limit at 12 MHz and 20 MHz appears to be approximately 0.006" and 0.003", respectively. Equation 3 predicts 0.044" and 0.026", respectively. It is worthwhile to note that during real-time observations, small flaws which are moving across the imaging screen are often easily detected while in a still photograph they are not. This is attributed to the eyes' ability to detect motion against a stationary background.

Reproduced from
best available copy.

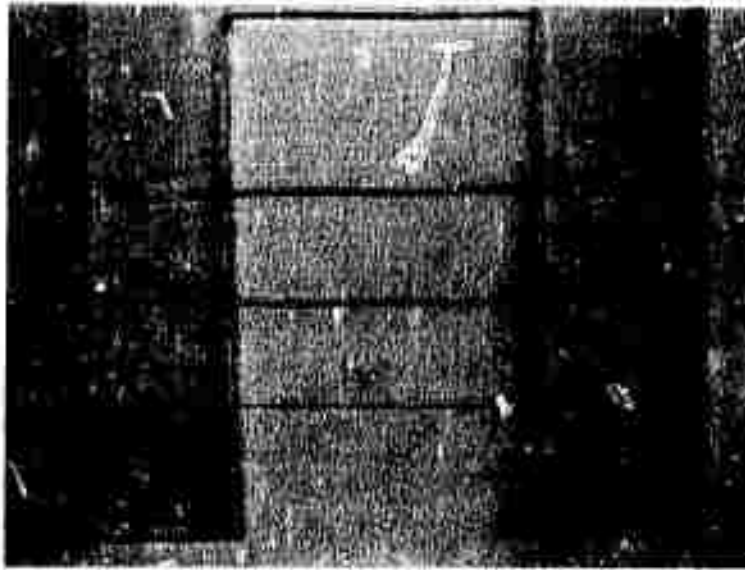


Figure 13: Stainless steel wires used to determine minimum detectable flaw size. Wire diameters from top to bottom are 0.008", 0.006" and 0.003".

THREE-DIMENSIONAL CHARACTER OF A FLAW

The two-dimensional image produced by the acousto-optical imaging technique is, in effect, a silhouette of the specimen against the irradiating acoustic transducer. This is analogous to the two-dimensional projection of the interior of the human body which is made using x-rays. Hence, as the specimen is rotated, different projections are produced indicating that the full three-dimensional character of a flaw may be determined by taking images of the specimen at more than one angle. In this section, it is shown that this is indeed the case.

First to illustrate the fact that different projections can be obtained by rotating the specimen with respect to the transducer, a simple experiment was performed. For this purpose an aluminum specimen was fabricated containing two sets of holes drilled into it. These holes lie in planes parallel to the surfaces of the specimen. One set consists of two holes lying in a common plane and intersect to form a "V". The third hole lies in a different plane and passes below the

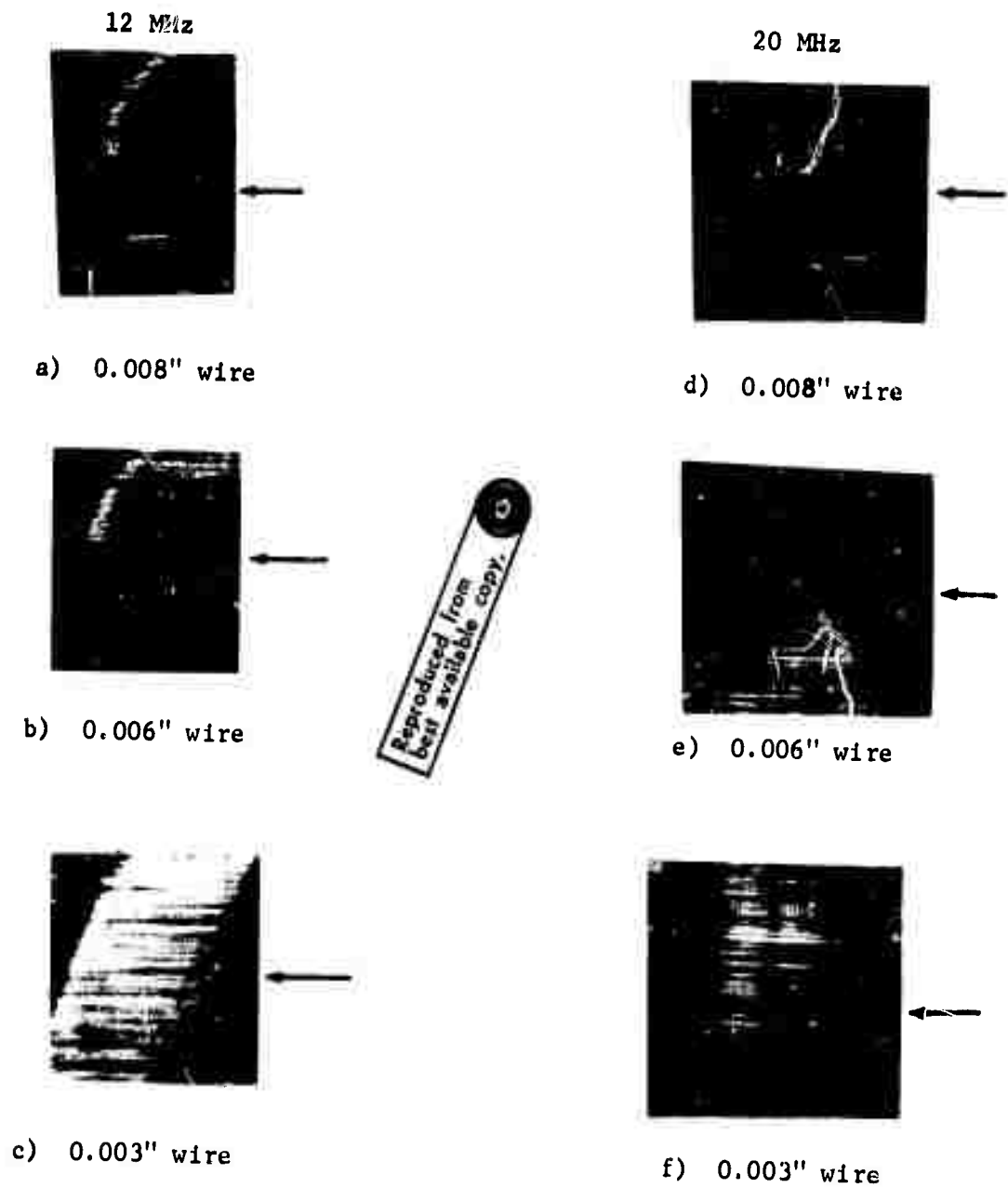


Figure 14: Acousto-optical images of three small diameter stainless steel wires using 12 MHz and 20 MHz ultrasound.

intersection of the other two holes as depicted in Figure 15. Figure 16 shows three images of the holes which correspond to three different orientations of the specimen with respect to the plane of the transducer. As one can see from the figure, the relative position of the single hole with respect to the "V" changes as the orientation of the specimen with respect to the transducer changes, thus illustrating that rotation of the specimen allows different projections of internal flaws to be obtained. This type of information can be used to obtain three-dimensional size information regarding the flaw as illustrated below. To demonstrate that the three-dimensional character of a flaw can be obtained from a

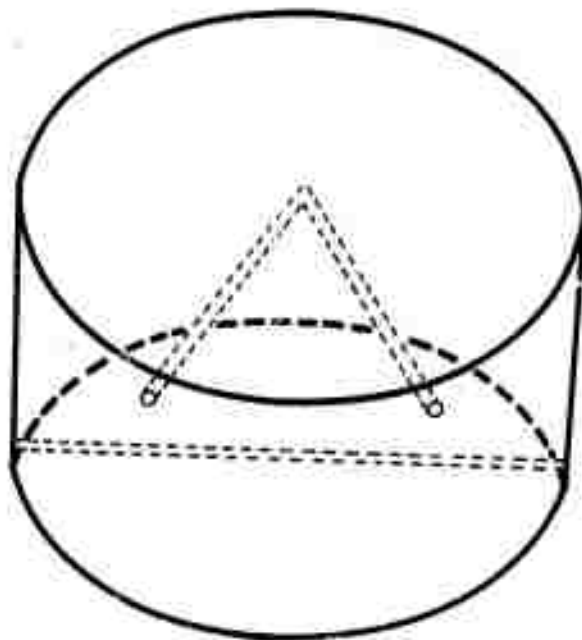


Figure 15: Specimen used to demonstrate that different projections can be obtained by rotating the specimen.

one-sided view, a specially prepared specimen was fabricated containing a known flaw. The flaw consisted of a cut made into the side of an aluminum plate using a circular saw. The width of the cut was 0.0245" and extended to a maximum depth of 0.250". Two acousto-optical images were obtained of this specimen using 20 MHz sound. Figure 17 shows the relative orientations of the specimen with respect to the transducer and the resulting image. The first image, shown in Figure 17c, was obtained with the cut oriented perpendicular to the plane of the transducer. The second image, Figure 17f, was obtained after rotating the specimen

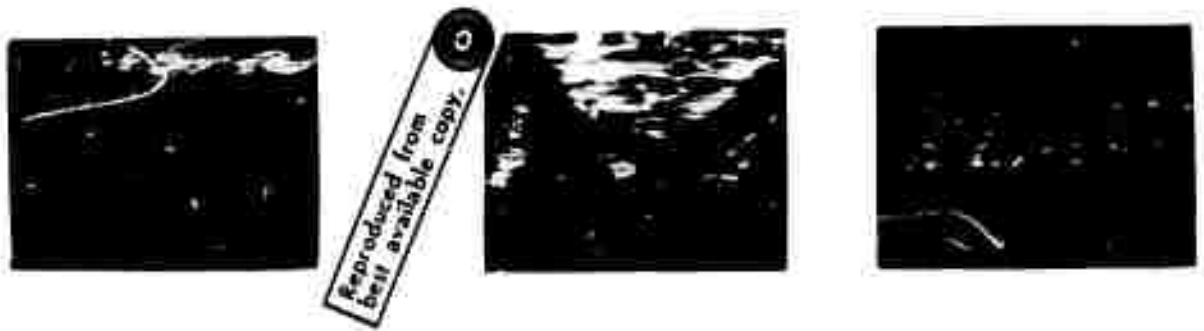


Figure 16: Images of specimen illustrated in Figure 15. These images correspond to three different orientations of the specimen with respect to the transducer.

through an angle of $5^{\circ} 12'$. To determine the size of the flaw from the acousto-optical image the procedure outlined in Section 3.0 was followed. The magnification of these photos was determined by comparing the actual width of the cut to its image, viz

$$M = \frac{\text{Image Size}}{\text{Actual Size}} = \frac{0.10 \pm 0.005''}{0.0245'' \pm 0.0005''} = 4.1 \pm 0.3$$

Using this magnification factor, the projected depth of the cut as measured from the image is

$$C = \frac{0.22'' \pm 0.01''}{4.1 \pm 0.3} = 0.054'' \pm 0.006''$$

From this measured projection and the known angle of rotation of the specimen, the depth, h , of the cut can be calculated by the equation

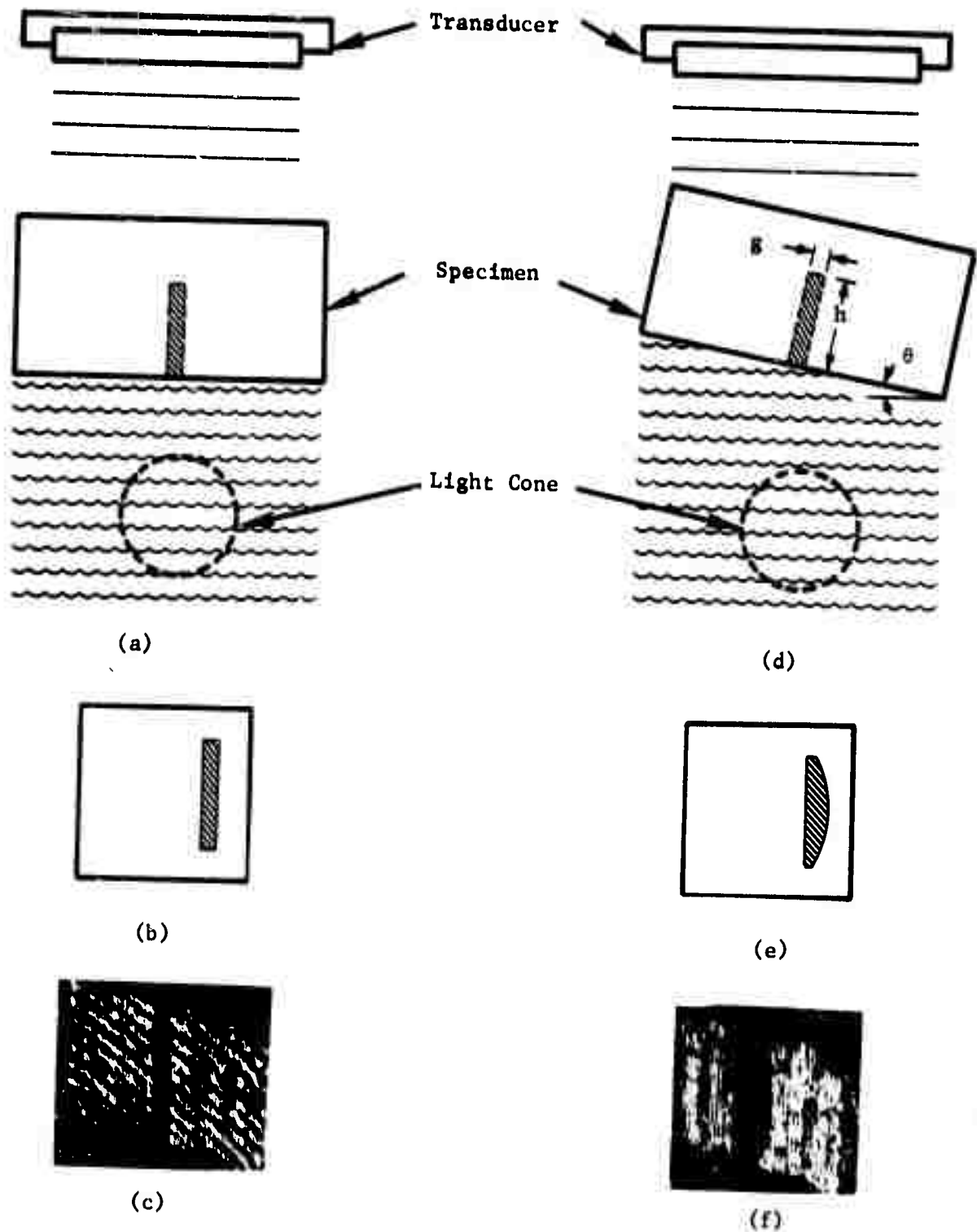


Figure 17: Schematic representation of technique to determine the three dimensional character of a flaw. Two orientations of the specimen with respect to the acoustic transducer and the light cone are shown in a) and d). The corresponding expected AOI images are drawn in b) and e). Actual AOI images for a specimen in each orientation are shown in c) and f).

$$h = \frac{C - g \cos \theta}{\sin \theta}$$

$$= \frac{(0.054'' + 0.006'') - (0.0245'' + 0.0005'')(0.9959 + 0.0001)}{(0.0906 + 0.0003)}$$

$$= 0.33'' \pm 0.08''$$

This calculated depth of the crack is ~ 32% higher than the known depth of 0.250". However, the error band for the acousto-optical discrepancy may be due to the acoustic diffraction effects which were neglected in this calculation. Nevertheless, it can be concluded that the approximate three-dimensional size of the flaw can be determined in addition to its geometry.

SURFACE ROUGHNESS

Most of the tests for this study were conducted using specimens having smooth flat surfaces. In this way, the condition of the surface would not be a factor in the evaluation of an image of an internal flaw. As with other imaging systems, superior images are obtained when the specimen has smooth flat surfaces. In nondestructive testing applications, however, it is more general to encounter specimens having varying degrees of surface roughness. For this reason, a series of tests were conducted to determine the effect of surface roughness on the acousto-optical imaging technique.

The surface roughness, or microfinish, of a machined part refers to the geometric irregularities on the surface which are a consequence of the machining process used. The markings or pattern on the surface are different for each type of tool or machining operation. The standard unit for surface roughness measurement is the arithmetical average deviation from the mean, measured in microinches ($1 \mu'' = 0.000001''$), taking into account all variations in the surface geometry.⁷

An aluminum specimen was fabricated on which was machined (end milled) four different grades of surface roughness, Figure 18. The microfinish on each of the four areas was measured using a Bendix Micrometrical Mode 4 Profilometer. The microfinishes of these four areas measured a) 45 microinches; b) 225 microinches; c) 300-350 microinches; and d) 300-400 microinches. These range from a fairly fine machine finish, (a), to a very rough finish, (d). Beneath each of these four areas, two .028" diameter holes, spaced .028" apart, were drilled from the side of the specimen, Figure 18. Images obtained of each of these sets of holes using 20 MHz and 40 MHz ultrasound are shown in Figure 19. As one may expect, a degradation of the image quality is evident in those areas having rougher surfaces; however, the flaws can still be detected in those areas. The images are also noticeably degraded at the higher frequency. One explanation for this is that there is a critical surface

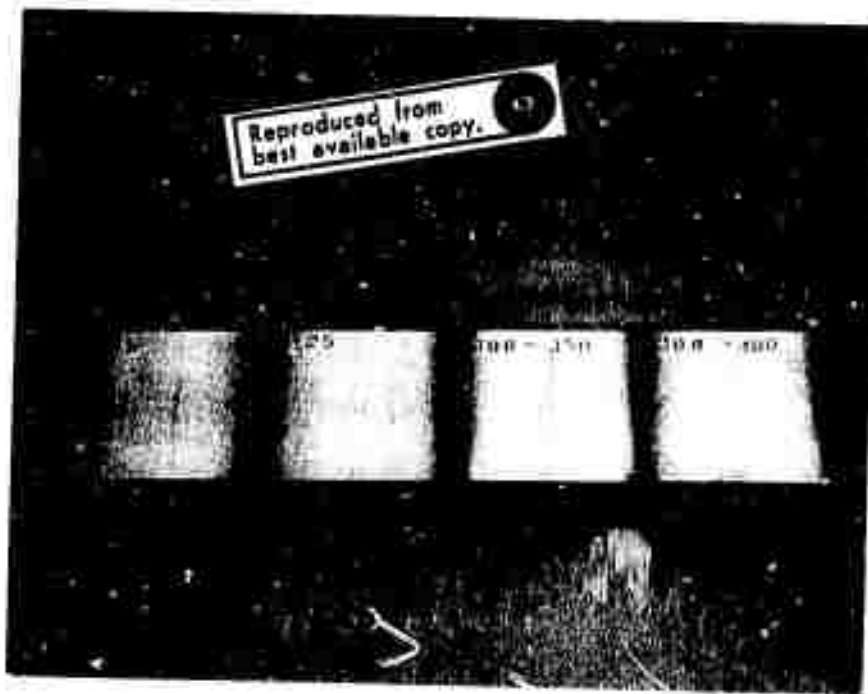


Figure 18: Surface roughness specimen. The numbers on the specimen indicate the roughness of the machined surface on each section of the specimen.

roughness value at which a null in the acoustic field is produced.⁸ This is a consequence of the differences in the acoustic velocities in the specimen and in the surrounding water. In the vicinity of the surface, the sound is traveling through both water and metal simultaneously. A phase difference between the two waves is produced which effects a decrease in acoustic energy when the waves recombine. The critical roughness, R_c , for which this destructive interference occurs is given by⁽⁸⁾

$$R_c = \frac{\lambda_s v_w}{2(v_s - v_w)} = \frac{\lambda_w v_s}{2(v_s - v_w)} \quad (6)$$

where

λ_s = acoustic wavelength in specimen

λ_w = acoustic wavelength in water

v_s = velocity of sound in specimen

v_w = velocity of sound in water

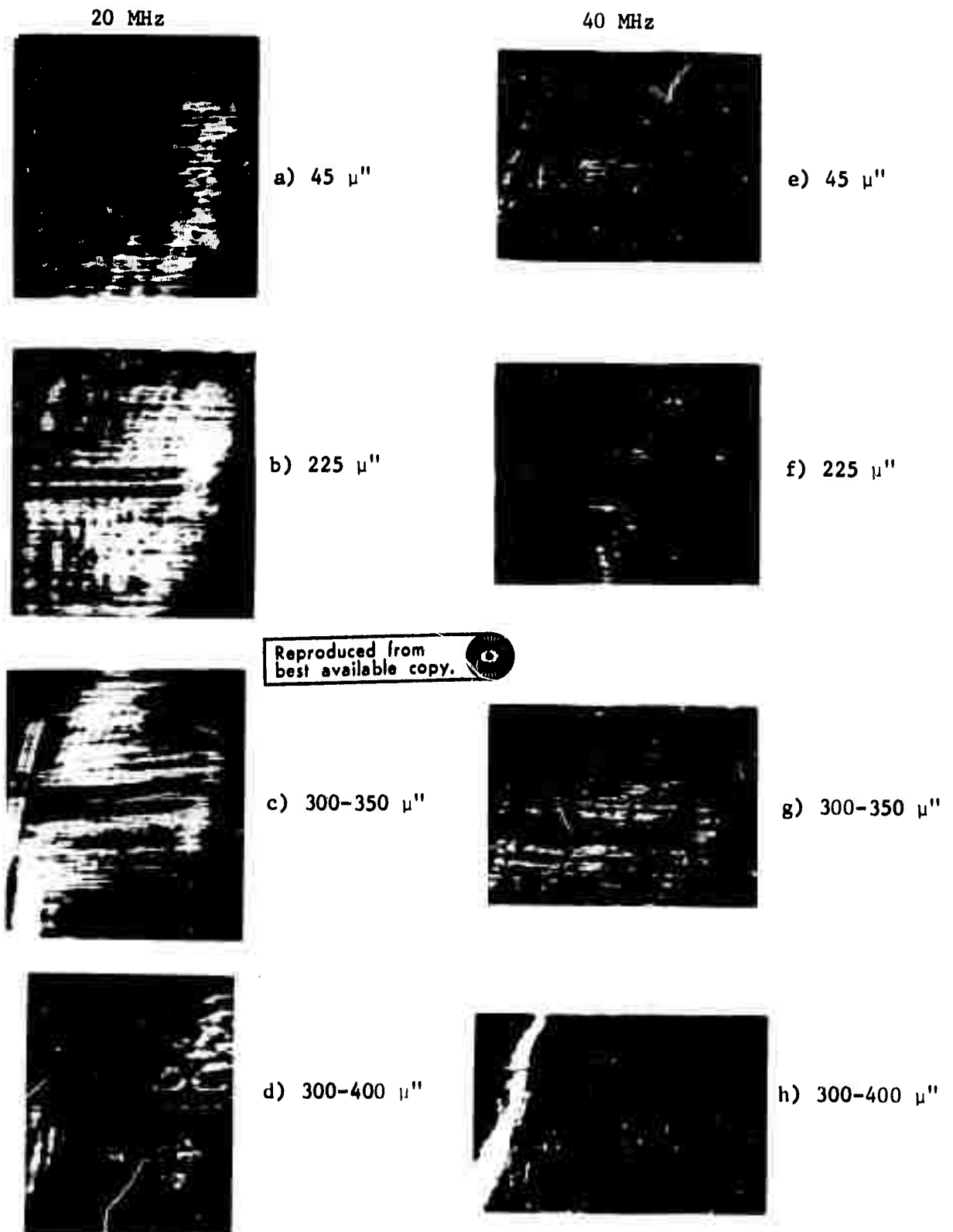


Figure 19: AOI images of two 0.028" diameter holes drilled into aluminum specimen 0.028" apart. The surface roughness (measured in microinches) of the specimen in the area of each set of holes is indicated along side each figure.

For an aluminum specimen, the critical roughness is $750 \mu''$ and $375 \mu''$ at 20 MHz and 40 MHz, respectively. Since our surface conditions are less than $750 \mu''$, one would not expect to see a pronounced effect on images taken at 20 MHz. However, at 40 MHz, the two roughest surfaces, Figures 19g and 19h are near the $375 \mu''$ critical roughness condition. At those roughness levels, the images are very poor, however, it is still possible to detect the flaw. It is worthwhile to note that this is a situation where real-time observation has a significant advantage over the photographic record of the flaws. When the specimen is rotated, the flaw is seen to move with respect to the shading caused by the rough surface. It is then easy for the observer to recognize the flaw and to determine that it is in fact interior to the specimen.

The surfaces on the specimen used here cover the range from fairly smooth to much rougher than would normally be encountered on a machined surface. The 0.028" diameter hole represents a fairly small flaw but by no means the resolution limit for this acoustic frequency (see Section 3.0). It may be reasonable to expect that a smaller flaw would be more easily masked by the surface roughness.

SPECIMEN GEOMETRY

An important factor in producing good images with an acoustical system is the geometry of the specimen, i.e., its size and shape. It is difficult to transmit sound through specimens having irregular shapes because of reflection and refraction of the sound at the surfaces. Large specimens are often difficult to properly orientate and may also greatly attenuate sound. For this study, emphasis was placed on curved surfaces in a geometry problem which is frequently encountered in nondestructive testing. In particular, segments of thick walled, cylindrical shells were considered.

Curved surfaces of shells act as acoustical lenses in that they focus sound passing through them. The focused sound interacts with the light in the Bragg cell resulting in a focused image. Since both surfaces curve in the same direction, the lens would be relatively weak if it were not for the large difference in sound speed between the aluminum specimen and the surrounding water. Using the appropriate equations for thick lenses, the acoustic focal length can be calculated for these shells. The focal length, F , is given by

$$F = \frac{R(R + t)}{2t} \quad (7)$$

where R is the inner radius of the shell and t is its thickness.

Cylindrical shell segments were fabricated having three different inner radii, viz., 3", 2" and 1-1/2". The orientation of the specimens with respect to the transducer and light cone for these tests is shown in Figure 20. For each radius, three shells were made having different wall thicknesses, viz, 1/8", 1/4" and 3/8". These nine specimens are shown in Figures 21 through 29. Each figure is labeled with the inner radius, thickness, and acoustical focal length (calculated using Equation 7) of the specimen. As in other parts of this study, two 0.028" diameter holes were drilled into the sides of the specimens. The holes were separated by one hole diameter. These holes are visible in the figures. Two acoustic-optical images were then obtained of each specimen. One was obtained with the specimen positioned so that the two drilled holes were opposite the center of the transducer as shown in Figure 20. Those images are shown for each specimen in the (b) part of Figures 21 through 29. The second set of images were obtained after the specimen was rotated about the axis of the shell. This resulted in images of an unflawed section. These images are shown in the (c) part of Figures 21 through 29. The focusing caused by the curved specimens is evident in these figures. The center of each image is fairly clear, however, the top and bottom is distorted. For the specimens having the shorter focal lengths (i.e., stronger lenses) the center area is narrower and the distortion at the top and bottom is much worse. The images of the holes in parts (b) of Figure 21-29 degrade considerably at the shorter focal lengths making it difficult to distinguish the separate holes as in Figures 28b and 29b. In the (c) parts of the figures, the holes are opposite the top of the transducer and are seen as rectangular black squares near the top of some of the images, as in

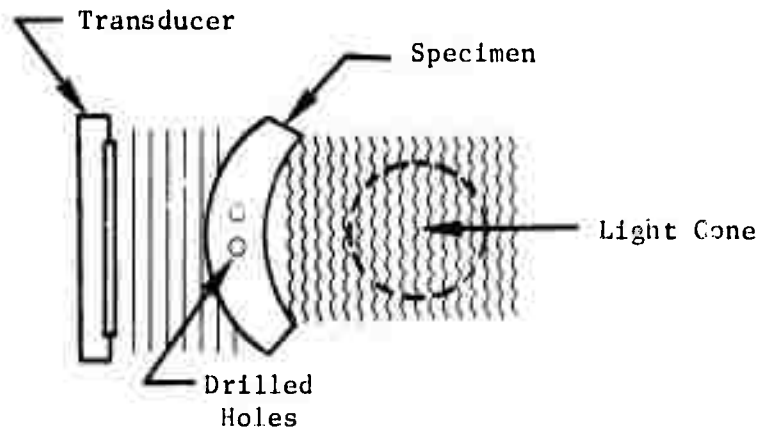


Figure 20: Relative orientation of the curved specimen with respect to the acoustic transducer and the light cone



(a)



(b)



(c)

Figure 21: Inner radius = 3"
Thickness = 1/8"
Focal Length = 37-1/2"

Reproduced from
best available copy.



Drilled Holes



(a)



(b)



(c)

Figure 22: Inner radius = 3"
Thickness = 1/4"
Focal Length = 19-1/2"



(a)



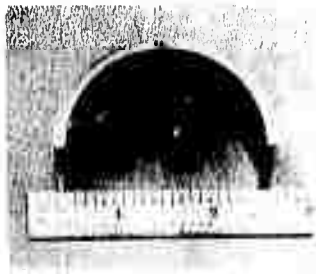
(b)



(c)

Figure 23: Inner radius = 3"
Thickness = 3/8"
Focal Length = 13-1/2"

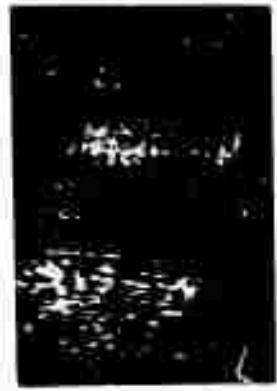
Drilled Holes



(a)



(b)



(c)

Figure 24: Inner radius = 2"
Thickness = 1/8"
Focal Length = 17"



(a)



(b)



(c)

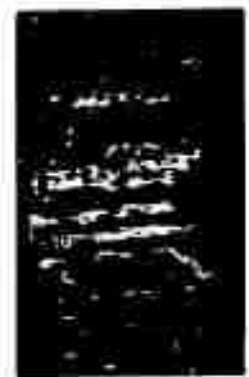
Figure 25: Inner radius = 2"
Thickness = 1/4"
Focal Length = 9"



(a)



(b)



(c)

Figure 26: Inner radius = 2"
Thickness = 3/8"
Focal Length = 6-1/3"



(a)

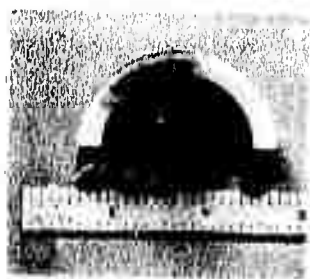


(b)



(c)

Figure 27: Inner radius = $1\frac{1}{2}$ "
Thickness = $\frac{1}{8}$ "
Focal Length = $9\frac{3}{4}$ "



(a)

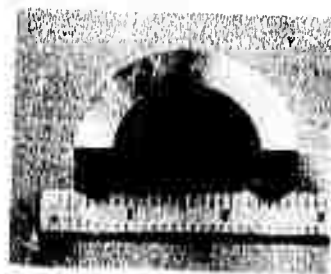


(b)



(c)

Figure 28: Inner radius = $1\frac{1}{2}$ "
Thickness = $\frac{1}{4}$ "
Focal Length = $5\frac{1}{4}$ "



(a)



(b)



(c)

Figure 29: Inner radius = $1\frac{1}{2}$ "
Thickness = $\frac{3}{8}$ "
Focal Length = $3\frac{3}{4}$ "

Figures 22c and 24c. It was not possible to resolve the individual holes when they were not oriented opposite the center of the transducer.

Attempts were made to fabricate acoustic lenses which would counteract the focusing effect of the specimens and thus enhance the image quality. These tests did not produce satisfactory results. The acoustic attenuation was very high due to the increase in the number of aluminum-water interfaces. Fabrication and positioning of the acoustic lenses is very critical. With further development, this technique may become feasible, however, it would most likely be limited to use with specimens having relatively simple geometries.

COMPOSITE SPECIMEN

Techniques of bonding composite materials have recently seen widespread industrial application, particularly in the aerospace industry. It has thus become increasingly important to be able to predict the performance of these materials using nondestructive techniques. The following test was designed to assess the ability of the acousto-optical technique to detect unbonded areas. A flat piece of plexiglas was bonded to aluminum using an epoxy resin, Figure 30a. The resin was colored to aid the photography. An area in the center of the specimen contained no resin (shiny area Figure 30a) thus producing an unbonded area. Figure 30b shows the acousto-optical image obtained of this specimen. Less sound was transmitted through the unbonded areas making them plainly visible. Traditional ultrasonic techniques (i.e., pulse reflection) can also detect this sort of flaw, however, these techniques require tedious mapping to determine the extent of the flaw. The ability of the acousto-optical system to provide the operator with an image of a large area of the specimen in real-time is a significant factor in fast, efficient bond inspection.

Reproduced from
best available copy.

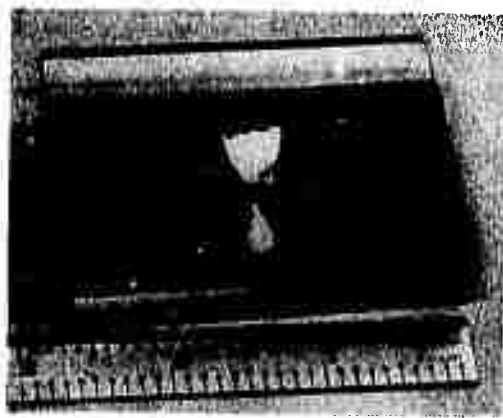


Figure 30: a) Composite bond specimen. Shiny area in center is unbonded
b) Acousto-optical image of the unbonded area

ACOUSTIC MICROSCOPE

The present study has dealt with the detection and imaging of relatively large flaws. The extension of these acousto-optical techniques to resolve smaller flaws is desirable for a number of nondestructive testing applications. Towards this end, a modification of the present system has been considered to increase the resolution of the system.

Equation 3 suggests two ways in which the resolution might be improved, i.e., by increasing the angle of the light cone and by increasing the acoustic frequency. Consider first the light cone angle since it is a parameter which is generally fixed by the hardware design. Practical considerations (e.g., difficulty in manufacturing low f-number lenses) place limits on the light cone angle. The dependence of the resolution limit on cone angle is shown in Figure 31. Although this curve shows ϕ out to a value of 3 radians, it is impractical to form a cone of this angle. On the other hand, a cone angle of 0.92 radians is easily achievable using an f 1.0 lens to focus a collimated beam. From Figure 31, it is seen that the resolution at 0.92 radians is only about a factor of three less than that obtainable with a light cone angle of 3 radians. This difference can be offset by increasing the acoustic frequency by a factor of three. The cost of increasing the acoustic frequency would be less than the cost of designing special lens systems making the former the preferred approach. The size of this cone is limited by the practical limitation of the size of the focusing lens. The overall size of the Bragg cell could be kept small thus allowing the use of a small lens. Inserting the cone angle of .92 radians into Equation 3 results in

$$d = \frac{2n}{\pi \phi} \lambda$$
$$= 1.8 \lambda. \quad (8)$$

One major limitation on using very high acoustic frequencies in water is attenuation. The acoustic attenuation factor is proportional to the square of the frequency so that the attenuation at 100 MHz is 100 times that at 10 MHz. The use of a small Bragg cell is again advantageous here so that the path length of the sound in water can be kept to a minimum. It appears that frequencies on the order of 150 MHz would be feasible. Figure 32 presents Equation 3 in graphical form. The resolution is given as a function of acoustic frequency for various cone angles. From this graph it is seen that the resolution limit of $\sim 7.2 \times 10^{-4}$ in. can be obtained when the acoustic frequency is 150 MHz and an f1.0 lens is used. This is approximately a factor of 20 better than that which is achievable with the system used during this investigation. As discussed above, it would be expected that the detectable flaw size would be smaller than the minimum resolution calculated here.

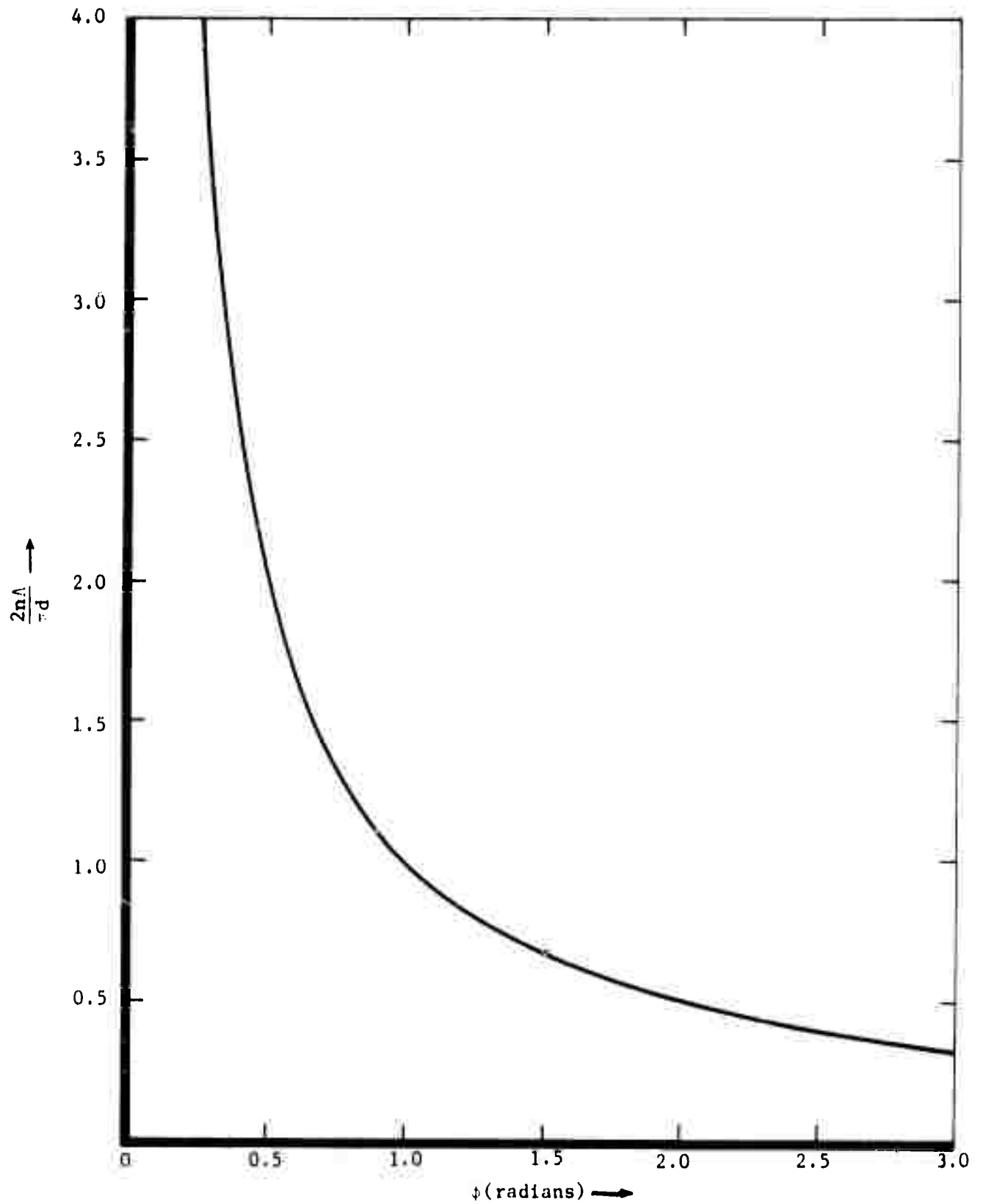


Figure 31: Plot of Equation 3 showing the dependence of the resolution limit on the light cone angle.

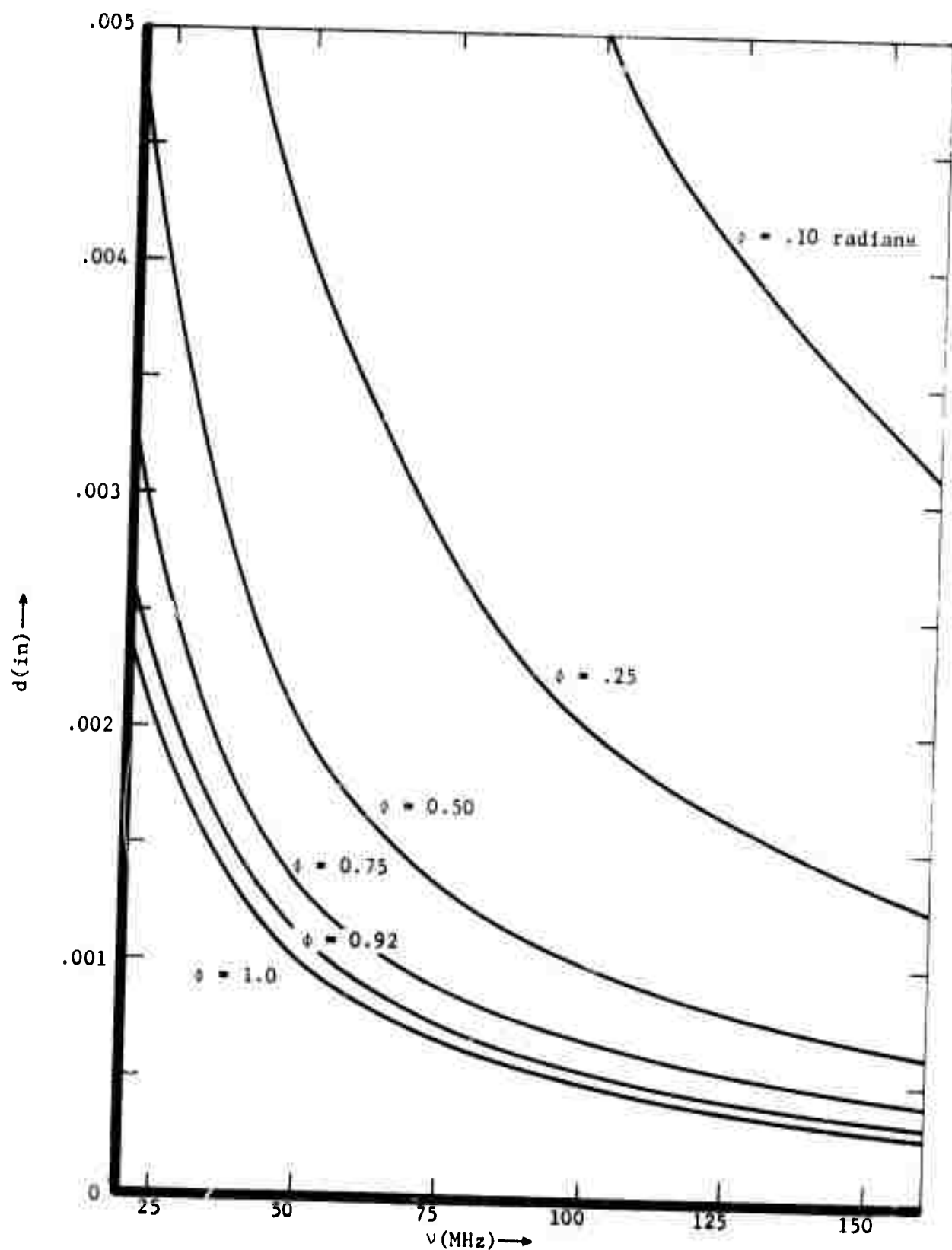


Figure 32: The dependence of the resolution limit on acoustic frequency for various light cone convergence angles.

REFLECTED SOUND IMAGING

The foregoing sections pertained to using sound waves which are transmitted through the material for nondestructive inspection. In many instances both sides of the specimen are not accessible nor is it permissible or practical to immerse the part to be inspected in a suitable wavecoupling medium. In such cases, it is desirable to devise means to inspect parts from one side. Preliminary experiments have been performed at TRW Systems Group using sound which is reflected from an object to cause Bragg diffraction of light. The experimental procedure can be described using Figure 33. Although immersion is required in Figure 33,

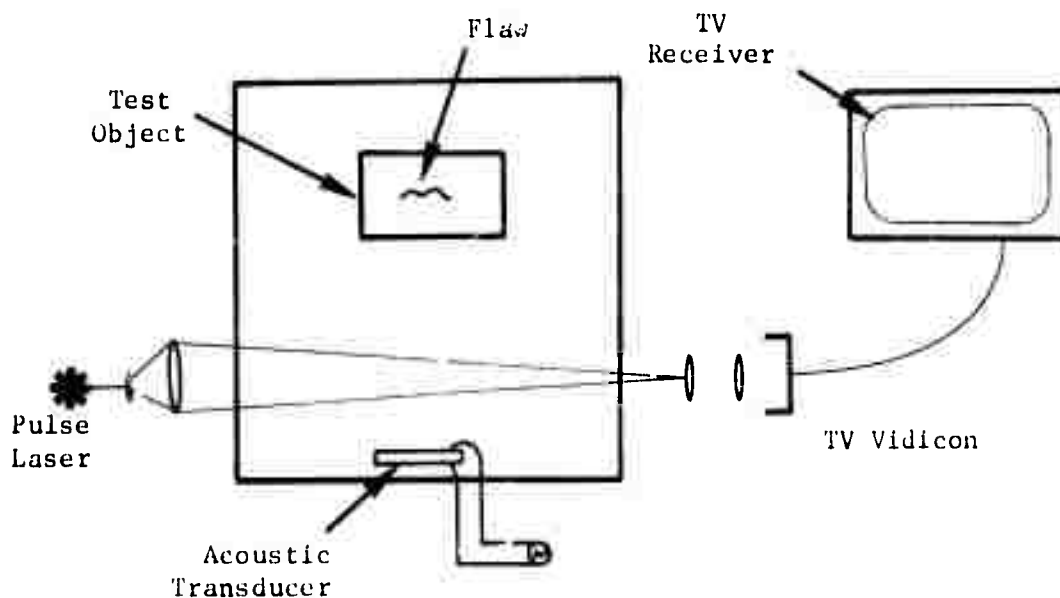


Figure 33: Set up to obtain images of defects using reflected sound to cause Bragg diffraction

the same principles can be applied to a non-immersion system. The basic system is similar to the one used in the transmission case except that the specimen is not placed between the sound source and light cone but on the other side of the light cone; pulsed light and pulsed sound sources

are used rather than continuous wave sources. A pulsed oscillator provided sound pulses of 25 μsec duration at a rate of 60 pps. The laser was a TRW Instruments pulsed argon laser ($\lambda = 5145\text{\AA}$ and 4880\AA) producing pulses of 40 μsec duration at a rate of 60 pps. While the duty cycle is very low for this mode of operation, the higher peak powers obtained from both the light and sound sources combine to produce an average image intensity only slightly less than in the cw mode when a 15 mw laser is used. Pulsing the sound source also prevents the occurrence of standing waves in the tank.

It was necessary to initiate the light pulse after the sound so that both the light and sound would arrive at the interaction volume simultaneously. The oscillator provided a delayed trigger signal which was used to trigger the laser. This delay is continuously variable from 2 μsec to 2 msec. Referring to Figure 34, a delay of $t = A/v$, where v represents the velocity of sound in water, would allow the sound coming directly from the transducer to be imaged. At this setting, a specimen situated in region I could be inspected by the transmission method. By adjusting the laser delay to $t = (A + 2B)/v$, an image would be formed by the sound being reflected from a specimen in region III. (The delay due to the speed of light is negligible.)

Tests with this system were made using the transmission mode of operation so that the image quality could be compared with that obtained

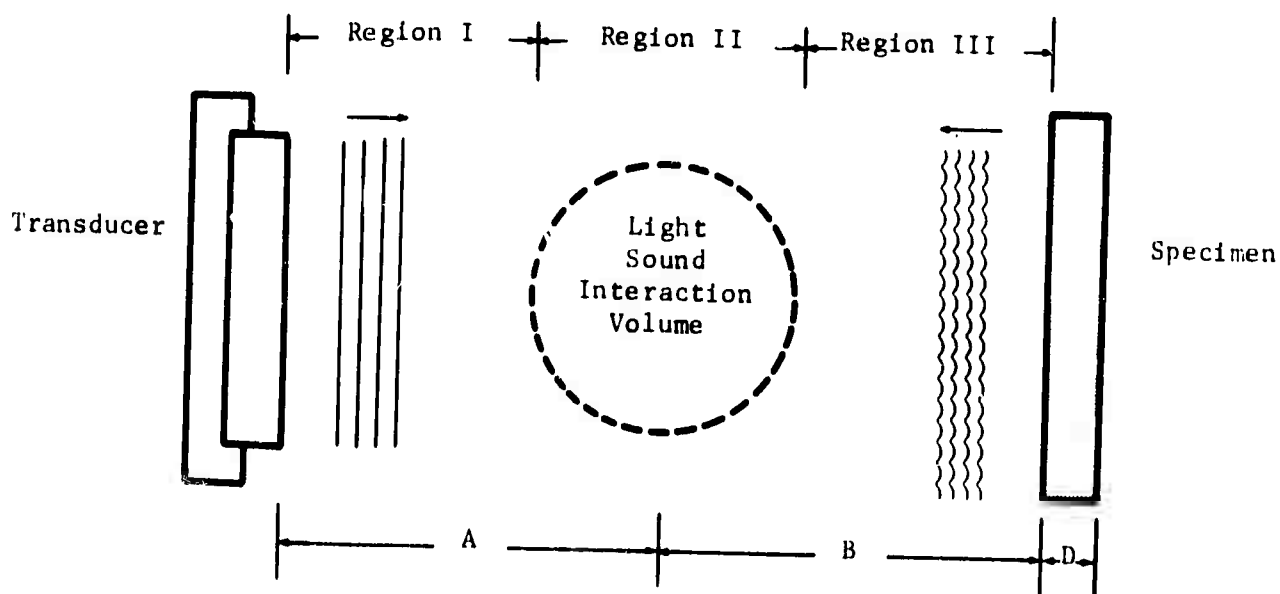


Figure 34: Experimental configuration for reflective sound imaging using pulsed light and sound sources.

using continuous wave light and sound sources. It was found that a double, or "ghost" image was obtained because of the two principal wavelengths of light present. The problem could be eliminated by filtering out all but the 5145Å component of the light. While the proper filter was not available in the laboratory, a filter was obtained which provided a usable image. The pulsed images appeared to have better contrast ratios than obtained with the cw mode. This is possibly due to the higher sound intensities which created a more efficient diffraction pattern. This also aided in imaging thicker materials in which the sound is attenuated. The only disadvantage encountered was the low overall intensity of the image. This problem was overcome by the use of a closed-circuit television system. The real acousto-optical image was projected directly onto the face of the vidicon tube of a television camera. The image was then viewed on a 21" diagonal television monitor. This not only produced a brighter image but the larger size enabled greater detail to be seen. Figure 35 shows the experimental setup with the closed-circuit television system.

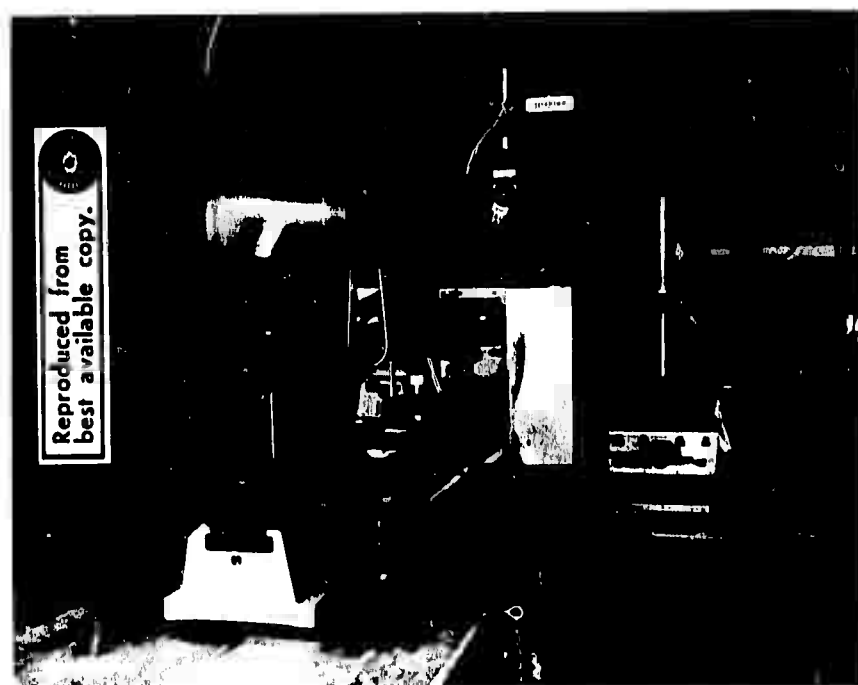


Figure 35. Experimental set-up showing closed-circuit television system

Using reflection techniques also facilitates the measurement of the thickness of the specimen. This can be accomplished by measuring the time between the arrival of the reflections from the front and rear surfaces of the specimen. Referring to Figure 34, it was shown above that an image of the front surface of the specimen would be obtained if the laser was delayed by $t_F = (A + 2B)/v$. If the laser delay is increased to $t_R = (A + 2B/v + 2D/v_s)$, where v_s is the velocity of sound in the specimen, then an image of the rear surface of the specimen would be obtained. The thickness can now be calculated using the measured time difference

$$\Delta t = t_R - t_F = \frac{2D}{v_s}$$

$$D = \frac{\Delta t v_s}{2}$$

This technique can be extended to measure the depth in the material of any anomaly which will reflect sound, i.e., a flaw.

Initial experiments using this pulsed light-sound reflection technique were performed using a rectangular strip of borsic aluminum containing a surface defect (Figure 36). Two images of the front

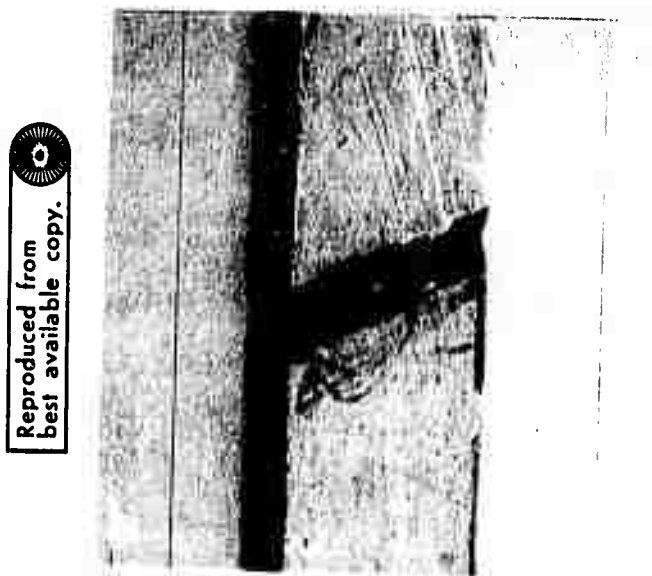
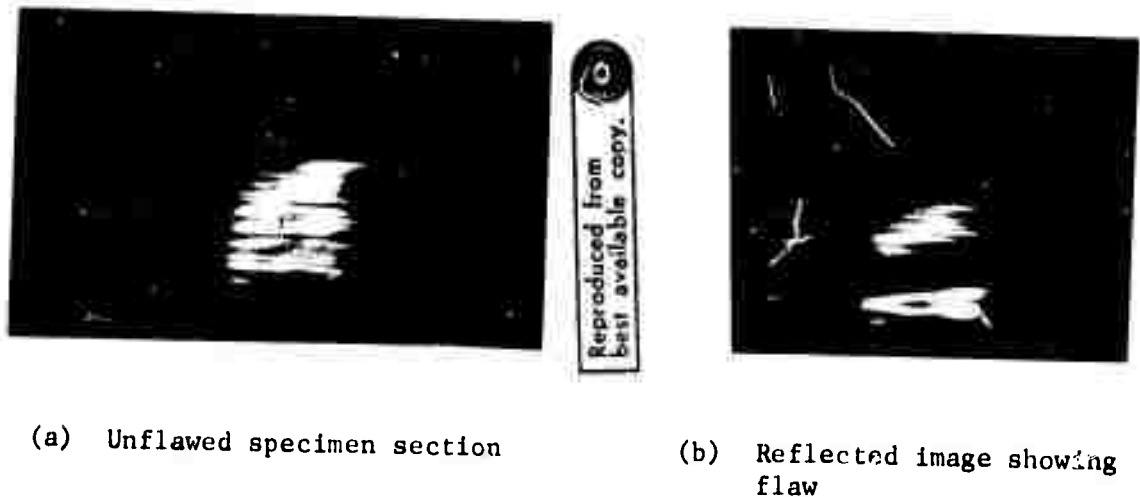


Figure 36: Flawed section of borsic aluminum specimen

surface of the specimen were obtained. The first was taken of the acousto-optical image of an unflawed portion of the specimen (Figure 37a) and the second of the flaw (Figure 37b). These pictures were taken from the television monitor which was displaying the images.



(a) Unflawed specimen section

(b) Reflected image showing flaw

Figure 37: Reflected sound images of specimen of borsic aluminum containing surface flaw

It is planned that further tests will investigate the applicability of these techniques to the imaging of internal flaws in the specimen. It is necessary to eliminate the acoustic wave which is reflected from the front surface of the specimen from that which carries the signal from inside the specimen. This requires that the acoustic pulse length ($\Delta L = v_s t$) be smaller than twice the flaw depth. Much shorter light pulse durations are required than used for the tests discussed above. To meet these requirements, future tests will be conducted using a pulsed xenon laser having very short pulse durations.

CONCLUSIONS

TRW's acousto-optical imaging system offers potential advantages in several nondestructive testing applications. This conclusion is based upon a series of tests which were performed to measure the resolution, the ability of the system to obtain information concerning the three-dimensional character of a flaw from a one-sided view, the effect of

surface roughness on the image, specimen geometry, and the ability to locate flaws in bonded composite specimens.

Theoretical predictions of resolutions were made and compared with the experimental results using carefully prepared control specimens in which the locations of the flaws and their dimensions were known. The resolution tests were performed at frequencies ranging from 4 to 40 MHz. The resolution increases with increasing acoustic frequency. The resolution is also a function of the light cone convergence angle. For the tests performed, the cone convergence angle was 0.093 radians. A larger cone angle will yield a higher resolution. The experimental test also showed that the acousto-optical imaging system could detect flaws which were only 1/10 of the size of those which could be resolved. "Resolution" is defined as the ability to distinguish a set of closely spaced flaws.

An analytical study to design an acoustic microscope based on the acousto-optical imaging technique was conducted. It was determined that using a light cone having a convergence angle of 0.92 radians and an acoustic frequency of 150 MHz will result (Equation 3) in a resolution limit of $\sim 7.2 \times 10^{-4}$ in. This is a factor of 20 better than that which is achievable with the system used during this investigation.

Preliminary tests were performed to obtain images using sound reflected from the object or flaw. To accomplish this, pulsed light and pulsed sound sources were synchronized so as to permit range gating. Using this technique, images of a surface flaw on the front side of a sample of boric aluminum were obtained.

REFERENCES

1. A. Korpel, "Acoustic Imaging by Diffracted Light, I. Two-Dimensional Interaction," IEEE Transactions on Sonics and Ultrasonics, Vol. SU-15, pp. 153-157, July 1968.
2. R. Adler, "Interaction Between Light and Sound," IEEE Spectrum, pp. 42-54, May 1967.
3. S. H. Bartley, "The Psychophysiology of Vision," Handbook of Experimental Psychology, edited by S. S. Stevens, John Wiley & Sons, Inc., New York, pp. 945-948, 1951.
4. N. E. Dorsey, Properties of Ordinary Water-Substance, Reinhold Pub., pg. 197, 1940.
5. C. S. Tsui and H. V. Hance, "Experimental Investigation of the Resolution Capability of Microwave Ultrasonic-Beam Visualization Technique Using Bragg Diffraction of a Laser Beam," J. Acoust. Soc. Amer. 48, 1110-1118, 1970.

6. M. Born and E. Wolf, Principles of Optics, Pergamon, New York, pp. 428-430, 1965.
7. J. Broadston, Control of Surface Quality, Surface Checking Gage Company, Hollywood, Calif., 1960.
8. R. C. McMaster, editor, Nondestructive Testing Handbook, Ronald Press, New York, p. 45 · 16, 1959.